Materials & Design 248 (2024) 113432

Contents lists available at ScienceDirect

Materials & Design

journal homepage: www.elsevier.com/locate/matdes

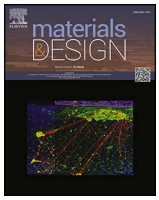

Design of transition metal carbide/nitride superlattices with bilayer period-dependent mechanical and thermal properties

Barbara Schmid [a,*], Thomas Schöngruber [a], Tomasz Wojcik [a], Bálint Hajas [a], Eleni Ntemou [b], Daniel Primetzhofer [b], Bernhard Fickl [c], Sarah Christine Bermanschläger [d], Szilard Kolozsvari [e], Nikola Koutná [a,f], Paul Heinz Mayrhofer [a]

[a] Institute of Materials Science and Technology, Technische Universität Wien, Wien, Austria
[b] Department of Physics and Astronomy, Uppsala University, Uppsala, Sweden
[c] Institute of Materials Chemistry, Technische Universität Wien, Wien, Austria
[d] Institute of Production Engineering and Photonic Technologies, Technische Universität Wien, Austria
[e] Plansee Composite Materials GmbH, 86983 Lechbruck am See, Germany
[f] Department of Physics, Chemistry and Biology, Linköping University, Linköping, Sweden

ARTICLE INFO

Keywords:
Carbide
Transition Metal
Mechanical Properties
Nitrides
Thin Films
Sputtering

ABSTRACT

Transition metal carbides are valued for high hardness, thermal and mechanical stability, but fall short in fracture toughness. Contrarily, their less hard transition metal nitride counterparts offer more favorable fracture characteristics. Here, we use magnetron-sputtering to synthesize nitrides and carbides—TiC/TaN, TiN/TaC—in a nanolaminate superlattice (SL) architecture and compare their properties (hardness, fracture toughness, thermal stability) with that of their layer materials, as well as of carbide SLs, TiC/TaC. Except for the monolithically grown TaN and TiC/TaN SLs with nominal bilayer periods above 14 nm, all other coatings are purely fcc-structured and feature close-to-stoichiometric compositions, revealed by EBS-ERDA and XRF measurements. In-situ X-ray diffraction investigations indicate that the monolithically grown coatings have poor thermal stability compared to the SLs, which remain stable up until well over 1000-°C. While the TiC/TaC superlattices retain the highest hardness of all three systems, with 44.1 ± 3.4 GPa at a bilayer period (Λ) of 2 nm, the TiN/TaC system exhibits significantly higher fracture toughness values with up to 4.75 ± 0.33 MPa$\sqrt{m}$ for the Λ = 14 nm coating. The TiC/TaN system exhibits neither hardness nor fracture toughness enhancement, as explained by the formation of a secondary hexagonal Ta_2N phase.

1. Introduction

Corrosion, wear, and limited resistance to crack initiation and propagation in engineering materials cause severe economic and sustainability issues due to the reduced lifetime of tools and other products. To enhance the surface stability of these materials, protective PVD coatings like TiN, (Ti,Al)N, or CrN have been applied since the 1980s [1]. This work focuses on ultra-high temperature ceramics (UHTCs), exhibiting melting points above 3000 °C [2]. UTHCs involve mostly binary compounds out of one (early) transition metal (TM) and one non-metal like B, C, or N. Offering high hardness and stiffness [3], UHTCs are perfect candidates for protective coatings and high-temperature applications. However, the major downside—especially for C-based UHTCs—is their low fracture toughness, leading to easy propagation of a pre-existing crack through the entire sample already at small strains. To avoid a catastrophic failure during operation, these materials need to be optimized (applying various design concepts, such as alloying or nano-laminated architecture) to exhibit initially hard but then reasonably ductile response to mechanical loads.

Superlattice (SL) architecture is a widely accepted concept for tuning the mechanical properties of transition metal nitrides [3,4]. Specifically, SL coatings consist of two or more materials at a nanometer scale, stacked alternatingly in a periodic manner. In general, different physical, chemical, and mechanical properties can be influenced by augmenting the bilayer period [4–7]. Chu and Barnett attributed the hardness enhancement to the disruption of dislocation gliding abilities [8]. Studies on various nitride SLs have been conducted to demonstrate the effect of bilayer period modulation on the hardness and fracture

* Corresponding author.
E-mail address: barbara.schmid@tuwien.ac.at (B. Schmid).

https://doi.org/10.1016/j.matdes.2024.113432
Received 7 May 2024; Received in revised form 31 October 2024; Accepted 4 November 2024
Available online 14 November 2024

behavior. For example, TiN/VN superlattices showed a hardness increase of ~150 % compared to the harder material, TiN [9]. Analogously, the combination of VC and TiC featured similar outcomes, resulting in a hardness of 41.9 GPa, which is a ~10 GPa increase compared to the harder material, TiC [10]. For various TiN-based nitride SLs (TiN/WN [5], TiN/MoN [7], TiN/TaN [11]) enhanced hardness and fracture toughness have been reported.

In contrast to well-researched nitride superlattices, relatively little has been reported on the even more covalent and brittle transition metal carbide superlattices. Our previous experimental and computational work indicated that both the hardness and fracture toughness of transition metal carbide coatings can be tuned by the superlattice architecture [13,14].

Recently, we were able to prove that a superlattice effect improving hardness and fracture toughness at the same time is also present in the superhard TiC/TaC system [13] and, to a certain extent, also in VC/HfC systems [14].

In this study, our primary aim is to further tailor properties of TiC/TaC SLs by exchanging either TiC or TaC with the corresponding nitride, if possible, i.e., by probing the concept or carbide/nitride superlattices, which may combine advantages of both material classes. Besides mechanical properties—typically the central point of SL studies—we perform a careful elementary analysis of the light elements (C, N) and correlate the trends observed with structural changes, thermal stability, and bonding properties.

2. Materials and methods

The coatings were deposited using a modified AJA Orion 5 deposition machine, which facilitates two 2-inch and one 3-inch cathode. Depending on the material system, we utilized a 3-inch TiC and 2-inch TaC, a 3-inch TiN and 2-inch TaC, or a 3-inch TaN and 2-inch TiC compound target. All targets were obtained from Plansee Composite Materials GmbH with a purity and density of ≥ 99.5 %. Nominal bilayer periods (Λ_{nom}) between 2 and 50 nm were adjusted via pneumatic shutter motion controlled by a Siemens Logo controller unit (the individual open times are based on pre-studies of the respective deposition rates). We used both Si (100) and austenitic steel substrates. The substrates were cleaned in an ultrasonic bath with acetone and ethanol for 5 min each. Before the deposition process, the chamber was evacuated to a base pressure below 10^{-3} Pa. After placing these substrates in the chamber using a load lock, they were Ar-ion etched for 10 min at 600 °C heater temperature, at an Ar pressure of 6 Pa, and a bias potential of −750 V. The depositions took place at a pressure of 0.3 Pa, an Ar flow of 15 sccm, a bias potential of −30 V, and 600 °C heater temperature. Targets were used in pulsed DC mode with power densities of 5.66–6.79 W/cm^2 for the 3-inch targets and 10.19–12.74 W/cm^2 for the 2-inch targets. The depositions started after a 3-min sputter cleaning the targets with these parameters.

The coating structure was determined via X-ray diffraction (XRD) investigations in symmetric Bragg-Brentano mode using Cu-K$_\alpha$ radiation (λ = 1.54 Å [15]), using a Panalytical XPert PRO MPD X-ray diffractometer.

The experimental bilayer period Λ_{exp} of the SL films was derived from the diffraction angle of the satellite reflexes θ_n and the cumulative reflex θ_{SL} using Eq. (1):

$$\frac{2sin\theta_n - 2sin\theta_{SL}}{\lambda} = \pm\frac{n}{\Lambda} \tag{1}$$

with λ representing the Cu-K$_\alpha$ radiation wavelength [Å] and n the order of the satellite reflexes. The strain-free lattice parameters d^0_{hkl} were calculated using following equation (2) [16]:

$$\varepsilon_{hkl} = \frac{d_{hkl} - d^0_{hkl}}{d^0_{hkl}} \tag{2}$$

Here, d_{hkl} refers to the lattice spacing derived from the diffractograms using Bragg's equation and ε_{hkl} to the in-plane residual strains derived from MOS investigations.

High-temperature in-situ XRD investigations were conducted on a Panalytical XPert MDP III X-ray diffractometer equipped with a BBHD mirror and an Anton Paar HTK 1200 N chamber in vacuum, with a base pressure of around 10^{-3} Pa, between 25 °C and 1200 °C.

The thickness and growth morphology of the individual coatings were examined via scanning electron microscopy (SEM) using a ZEISS Sigma 500 VP Field Emission Gun Scanning Electron Microscope (FEGSEM) at an acceleration voltage of 5 kV.

The microstructure of the coatings with small bilayer periods was investigated on an FEI Tecnai F20 transmission electron microscope (TEM) operated at 200 kV acceleration voltage in bright field (BF) and scanning (STEM) mode. STEM micrographs were acquired by a high-angle annular dark field detector (HAADF) for mass contrast. Selected area electron diffraction (SAED) was applied to analyze the crystal structure and texture of the coatings.

We derived depth profiles regarding the composition of all coatings via Time-of-Flight (ToF) Elastic Recoil Detection Analysis (ERDA). Our investigations were conducted on the 5 MV Pelletron Tandem accelerator at Uppsala University [17]. Heavy $^{127}I^{8+}$ ions at energies of 36 MeV and an incident angle of 67.5° were used to perform our investigations. The data was analyzed using the Conversion of Time-Energy Spectra (CONTES) program [18]. We estimate the statistic and systematic uncertainties that stem from plural scattering and uncertainties in the energy loss to be around 5–8 % of the individual values [19]. We further performed Elastic Backscattering Spectrometry (EBS) to reduce those uncertainties to a minimum. Here, we used $^4He^+$ ions at 4.35 MeV and employed the elastic $^{12}C(^4He, ^4He)^{12}C$ resonance at ~4.26 MeV and a detection angle of 170°. We varied the incident angle between 5 and 50° [20]. Using the insights from ERDA investigations, we utilized SIMNRA to create our EBS spectra [21].

We utilized RAMAN spectroscopy using a WITec alpha 300 RSA + RAMAN spectrometer at a laser wavelength of 532 nm and 20 mW of power, referencing an external SiO_2 standard. X-ray fluorescence (XRF) investigations with a Panalytical AXIOS appliance in both energy dispersive (EDXRF) and wavelength dispersive (WDXRF) mode in vacuum using a rhodium anode at ambient temperature. The EBS-ERDA measured samples served as the standards for calibrating these measurements.

Nanoindentation experiments using a UMIS by Fisher Cripps Laboratories ultra-nanoindentation system (equipped with a Berkovich indenter) were performed to obtain both indentation hardness H and modulus E of our coatings, following standard procedures for evaluating the load–displacement curves [22]. At least one set of 30 individual indentation experiments was carried out per sample, keeping the indentation depth below 10 % of the total coating thickness. The same system, but equipped with a cube-corner tip, was used to determine the apparent fracture toughness K_{IC} of the coatings, using Eq. (3) [23,24]:

$$K_{IC} = \delta\left(\frac{E}{H}\right)^{\frac{1}{2}} * \frac{F_m}{c^{\frac{3}{2}}} \tag{3}$$

Where δ refers to an empirical constant (being 0.035 and independent of the material [24]), F_m is the maximum load (which was varied between 50 and 450 mN), and c is the radial crack length (obtained from SEM measurements). Each set of measurements was carried out three times.

Stress analyses were carried out with a K-space Multi Optical Sensor (MOS) Thermal scan device in x-y scan mode at ambient pressure and temperature. From the measured curvature κ of the samples, in-plane film stresses σ_F were calculated using Stoney's equation [25,26]:

$$\sigma_F = \frac{\overline{M_s}h_s^2}{6h_F} * \kappa \tag{4}$$

where M_s represents the substrate's biaxial elastic modulus, $E/(1-\nu^2)$, h_S the substrate thickness and h_F the film thickness [26].

3. Results

3.1. Chemical composition

To determine the chemical analysis of our samples, we chose the EBS-ERDA and EBS-ERDA calibrated XRF techniques, which are detailed in the Methods section. We emphasize that measuring the content of light elements is a particularly challenging task. Especially when using X-ray-based techniques, the creation of Auger electrons and the low intensities and longer wavelengths of characteristic X-ray radiation tend to be absorbed quickly by the material itself, leading to a loss in sensitivity. Our TiC, TaC, TiN, all TiC/TaC SL thin film samples, and the TiN/TaC SL with $\Lambda_{nom} = 10$ and 50 nm samples were analyzed by EBS-ERDA, while all other coatings (TiC/TaN and remaining TiN/TaC SLs) were analyzed by ERDA-calibrated EDXRF and WDXRF.

Fig. 1 presents the chemical compositions of all SL coatings and the corresponding monolithically grown binary coatings (referred to as monolithic). Nearly all TiC/TaC SL coatings (Fig. 1, bottom) are stoichiometric, with metal contents between 49.1 and 50.8 at.-%. The $\Lambda_{nom} = 14$ nm SL exhibits the lowest metal content with 46.1 at.-%. As intended, the metal-to-metal ratios are also nearly 1:1, suggesting a symmetric bilayer arrangement. The TiN/TaC SLs are similar with slightly higher metal contents (between 54.7 and 55.6 at.-%) for $\Lambda_{nom} \leq 14$ nm and 50.2–50.3 at.-% for $\Lambda_{nom} \geq 28$ nm (Fig. 1, center). Here, the $\Lambda_{nom} = 2$ nm superlattice exhibits a slightly higher Ta content than Ti. While TiN and TaC are sub-stoichiometric regarding non-metals (44.4 to 45.9 at-%), TiC is slightly over-stoichiometric in C (55.1 at.-%). The monolithic Ta-N coating features a Ta-to-N ratio of 2:1, thus, we will refer to this as Ta_2N. Like the TiC/TaC SLs, the TiC/TaN SLs are rather stoichiometric with metal contents of 48.2 to 53.76 at.-%, especially for $\Lambda_{nom} \leq 28$ nm. The SL with $\Lambda_{nom} = 50$ nm exhibits a much higher Ta content of 34.5 at.-% (and a Ta-to-N ratio of 1.4), pointing towards an increased formation of hexagonal Ta_2N with increasing Λ_{nom} (and thus, increasing Ta-N layer thickness). Ta-N energetically favors the hexagonal hex-Ta_2N phase, while the face-centered cubic fcc-TaN is a high-temperature phase that forms at around 1500 °C [27]. Due to the template effect from the fcc-TiC, it is possible to stabilize the Ta-N as TaN, similarly to the stabilization of the metastable fcc-AlN in TiN/AlN SLs [28,29]. All data suggest that the SL arrangement also influences the preferred stoichiometry of the individual layers. This might be due to the forced fcc-phase formation for these arrangements, see next sub-chapter. We will also show that if the Ta-N sub-layers grow thicker (see TiC/TaN SLs with $\Lambda_{nom} \geq 28$ nm), the increasing faction of hexagonal Ta_2N also allows for a much higher Ta/N ratio.

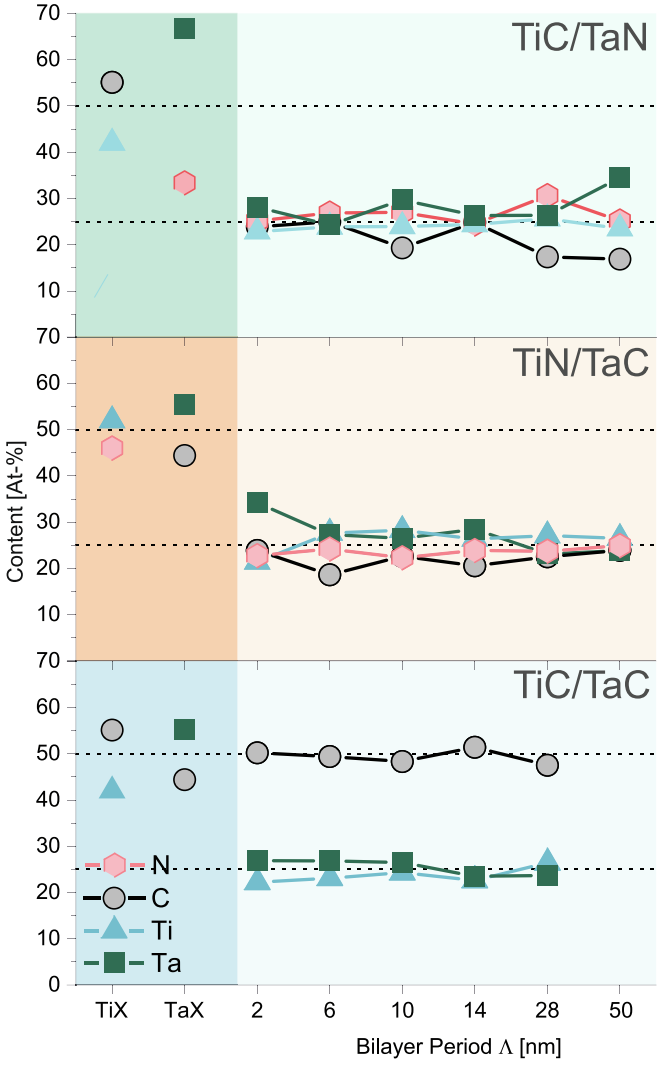

Fig. 1. Chemical composition of the TiC/TaC (bottom), the TiN/TaC (center), and the TiC/TaN (top) system, as determined using the EBS-ERDA measurements (TiC, TaC, TiN, all TiC/TaC SLs, and TiN/TaC SLs with $\Lambda_{nom} = 10$ and 50 nm) or ERDA-calibrated EDXRF and WDXRF measurements (TiC/TaN and remaining TiN/TaC SLs). Ta-based binaries are referred to as TaX, and Ti-based binaries as TiX (left part of bottom axis).

3.2. Structure

Fig. 2 compares XRD patterns of the monolithic films—TiC, TaC, TiN, and Ta_2N—with their SLs—TiC/TaC, TiN/TaC, and TiC/TaN. The SLs are additionally distinguished by their nominal bilayer periods, Λ_{nom} (2–50 nm), consistent with those derived from XRD measurements, Λ_{exp}, see Table 1. The TiC, TaC, and TiN coatings exhibit face-centered cubic (fcc; rock-salt) crystal structures, while Ta_2N features a purely hexagonal crystal structure [30]. TiC shows a strong preferred (111) orientation, TaC, and Ta_2N do not feature a preferred orientation, and TiN is strongly oriented in (200). There, lattice parameters, a, and stress-free lattice parameters, a_0, calculated from the stresses obtained from MOS investigations, are given in Table 1. For the calculation of the stress-free lattice parameters of fcc-structured materials, literature values for Poisson's ratios were used (0.25 for TiN, 0.19 for TiC, 0.21 for TaC) [33,34]. The comparison with theoretical (*ab initio* calculated) and other experimental values (Table 1) shows good quantitative agreement with our measurements. The reflex at $2\theta \approx 33°$ is the forbidden $\lambda/2$ reflex of the Si (1 0 0) substrate and has been discussed before for TiC and TaC films in Schmid et al. [13].

The multiple orders of satellite reflexes obtained from the SLs' diffractograms were used to calculate their bilayer periods, Λ_{exp}, using Eq. (1). The values are in decent agreement with the intended nominal periods, Λ_{nom}, see Table 1. Those satellite reflexes are exceptionally prominent for the $\Lambda_{nom} = 6$ and 10 nm superlattices and are further apart, the smaller the bilayer period gets. Our SL samples feature relatively broad reflexes due to their polycrystalline nature, which limits the resolution. For larger bilayer periods, the SL reflexes overlap with the cumulative zero-order reflex; see the $\Lambda_{nom} = 14$ nm SLs. The SLs essentially show a mixed 111- and 200-oriented growth, except for the TiC/TaN with $\Lambda_{nom} \geq 10$ nm, which yields a preference for 111-orientation. Generally, for larger Λ_{nom}, the layers can be detected more separately, rather than a cumulation with SL reflexes. This effect is apparent for the TiN/TaC and TiC/TaN materials with $\Lambda_{nom} = 28$ and 50 nm. The TiC/TaN materials with $\Lambda_{nom} \geq 28$ nm clearly reveal the presence of an additional hexagonal Ta_2N phase, forming within thicker Ta-N-layers (as obtained for the monolithically prepared Ta-N). Furthermore, we observe a loss of coherency strains with the fcc-TiC layers. Even for those

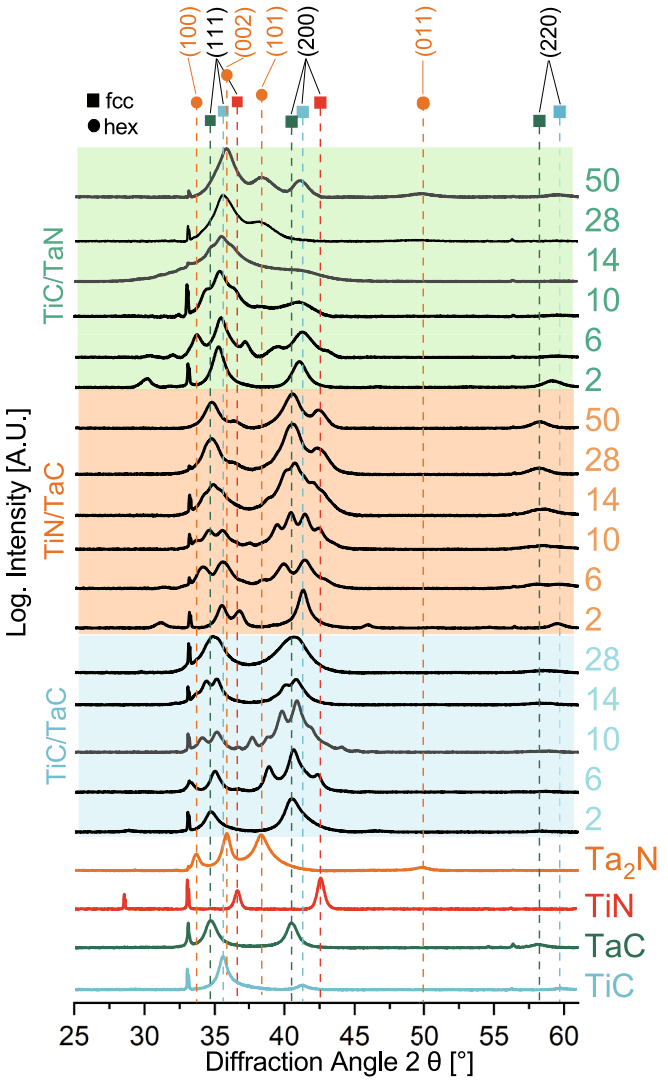

Fig. 2. X-ray diffractograms of the monolithic TiC, TaC, TiN, and Ta_2N coatings at the bottom and the corresponding TiC/TaC, TiN/TaC, and TiC/TaN SLs with labeled Λ_{nom} in nm.

we use the TiC/TaN nomenclature, however, keep in mind that the Ta-N layers for $\Lambda_{nom} \geq 28$ nm contain not only fcc-TaN but also hex-Ta_2N. This stoichiometry naturally changes the Ta/N ratio from ~ 1 (for small bilayer periods) to 1.4 for $\Lambda_{nom} = 50$ nm, compare Fig. 2. Even the SLs with $\Lambda_{nom} = 10$ nm and 14 nm show indications (by the small hump at $2\theta \approx 38°$) of an additional hexagonal Ta_2N phase.

3.3. Growth morphology

TEM bright field and STEM investigations of the superlattices with smaller bilayer periods, $\Lambda_{nom} = 2$ and 6 nm, show that the TiN/TaC and TiC/TaN SLs feature a nanolayered structure, Fig. 3a and b, respectively. These are similar to the TiC/TaC SLs already presented in Ref. [13]. Due to mass contrast in STEM mode, the brighter layers in the STEM images represent TaC and TaN, and the darker ones are TiC and TiN. The investigations show a dense growth morphology with relatively symmetric bilayer period arrangements (i.e., comparable thickness of the individual layers).

The selected area electron diffraction (SAED) insets of Fig. 3 confirm their single-phase fcc crystal structure. Since the samples with $\Lambda_{nom} = 2$ nm, Fig. 3a and b, show ring-shaped patterns without a distinct preferred orientation, the microstructure consists of nano-sized grains

Table 1
Comparison of nominal (Λ_{nom}) and XRD-derived bilayer periods (Λ_{exp}) for TiC/TaC, TiN/TaC, and TiC/TaN SL coatings and the comparison of the XRD-derived stress-free lattice parameters of the monolithic TiC, TaC, and TiN coatings with those from the literature, a_{lit}, (experimentally obtained) and previous *ab initio* density functional theory (DFT) calculations, a_{DFT}.

Material system	Λ_{nom} [nm]	Λ_{exp} [nm]	a_{lit} [Å]	a_{DFT} [Å]	a_{XRD} [Å]	a_0 [Å]
TiC	–	–	4.29 [34]	4.34 [35]	4.38	4.33
TaC	–	–	4.45 [36]	4.48 [35]	4.49	4.47
TiN	–	–	4.24 [34]	4.26 [35]	4.24	4.23
Ta_2N			a = 3.05 c = 4.92 [37]	a = 2.95 c = 5.57 [35]	a = 3.07 c = 5.78	–
TiC/TaC	2	1.66				
	6	5.71				
	10	9.76				
	14	–				
	28	–				
TiN/TaC	2	2.07				
	6	6.21				
	10	9.74				
	14	–				
	28	–				
	50	–				
TiC/TaN	2	1.60				
	6	5.32				
	10	9.01				
	14	–				
	28	–				
	50	–				

without texture or a distinct growth direction. The TiN/TaC sample with $\Lambda_{nom} = 6$ nm, Fig. 3c, shows a preferred growth orientation, and the TiC/TaN sample with $\Lambda_{nom} = 6$ nm, Fig. 3d, shows a preferential 111- and 200-growth orientation. In both samples with $\Lambda_{nom} = 2$ nm, Fig. 3a and b, and in the TiN/TaC sample with $\Lambda_{nom} = 6$ nm, Fig. 3c, the layers show a waviness. Also, the column boundaries are slightly visible. In contrast, Fig. 3d—which shows a region of the TiC/TaN SL ($\Lambda_{nom} = 6$ nm) closer to the substrate—exhibits flatter layers. It is commonly observed, that especially for polycrystalline SLs and multilayers, the waviness of the individual layers becomes more apparent with increasing coating thickness, partly stemming from the different crystallographic orientations of their columns.

3.4. Thermal stability

In-situ X-ray diffraction (XRD) combined with temperature stability analysis represents a powerful analytical approach that enables real-time investigations of structural changes in materials with temperature. These investigations were carried out for the SL coatings— TiC/TaC, TiN/TaC, and TiC/TaN, all with $\Lambda_{nom} = 10$ nm—as well as their monolithic components (TiC, TaC, TiN, Ta_2N). The corresponding data are given as heat maps in Fig. 4. Although the experiments were conducted in a vacuum, TiC (Fig. 4a) and TiN (Fig. 4b) started oxidizing around 750 °C. While TiC is completely oxidized at 1000 °C (as suggested by the missing reflexes for TiC), TiN can still be detected after the heating cycle to 1200 °C, along with TiO_2. The standard diffraction angle position of the anatase- and rutile-structured TiO_2 phases are indicated with purple round symbols marked with either an A or an R, respectively, and $TiSi_2$ is indicated with a fuchsia star [38,39]. The forbidden $\lambda/2$ reflex and K_β (400) reflex of the Si-substrate are marked with a grey square. Further, the TaC coating exhibits subpar adhesion to the Si substrate, which can also be derived from the cube corner indents

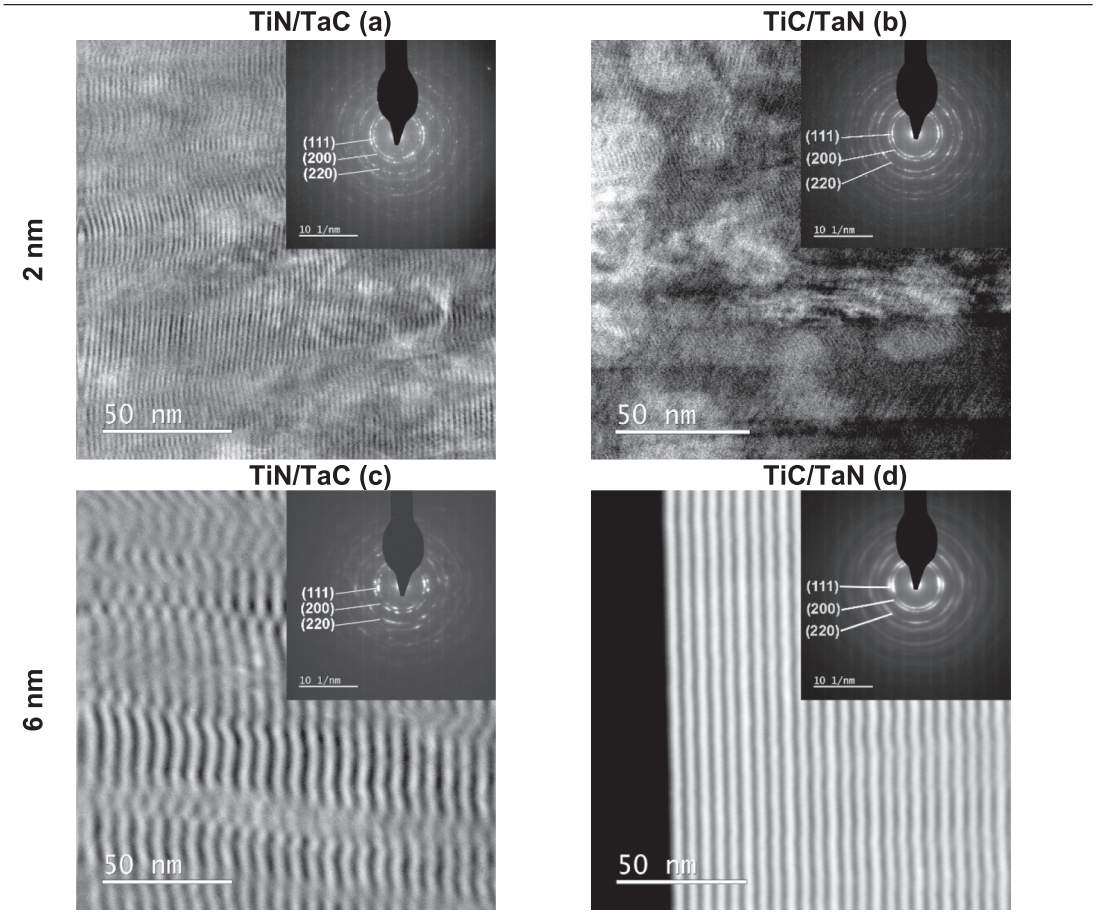

Fig. 3. STEM cross sections of (a) TiN/TaC $\Lambda_{nom} = 2$ nm, (c) TiN/TaC $\Lambda_{nom} = 6$ nm, (d) TiC/TaN $\Lambda_{nom} = 6$ nm, and (b) TEM BF cross-section of TiC/TaN SLs with $\Lambda_{nom} = 2$ nm. The insets are respective SAED patterns.

presented later. As a result, the films delaminate from the substrate at 900 °C (therefore, these XRD heat maps are not shown here). Ta_2N starts to oxidize at around 900 °C and is only fully oxidized at 1100 °C. At the same time, $TaSi_2$ (with its standard diffraction angle position marked with a green star) forms [40,41], see Fig. 4c.

Both TiC/TaC and TiN/TaC SLs feature excellent temperature stability, beyond their individual constituents TiC, TaC, and TiN. The onset of oxidation to form TiO_2 is in both cases at around 1100 °C, Fig. 4d and e, respectively. At even higher temperatures, Ta_2O_5 can be detected (see the standard diffraction angle position marked with orange hexagons) [42]. The comparison with the individual monolithically grown constituents suggests that the superlattice arrangement—besides allowing for improved mechanical properties—also enables an increased resistance against diffusion (which is necessary for oxidation). Contrary to the TiC/TaC and TiN/TaC SLs, the TiC/TaN SL starts to oxidize already at temperatures closer to those of the constituents TiC and TaN, at 825 °C, see Fig. 4f. The investigated TiC/TaN coating exhibits $\Lambda_{nom} = 10$ nm. A plausible explanation for this is the likely emerging hexagonal Ta_2N phase within the Ta-N layers, deteriorating the compactness and thus the resistance against diffusion of those coatings.

Interestingly, only the metastable anatase, not rutile, is formed for the SL systems and is still present after cooling. A further distinct difference between the monolithically grown coatings and the SLs is that the monolithic coatings tend to form disilicides due to the diffusion of Si into the coatings (the corresponding diffraction angles are marked with stars in Fig. 4a, b, and c). However, this phenomenon is absent in superlattice coatings, further confirming their previously noted higher resistance to diffusion. The absence of disilicide formation in the TiC/TaN superlattice, which was not that effective in retarding oxidation compared to the other two superlattices, suggests that its Ta-N layers closer to the Si substrate do not contain the disruptive hexagonal Ta_2N phase. This phase more readily forms further from the substrate (in the outermost regions of the entire coating), negatively impacting oxidation resistance. This observation aligns with the fact that thicker Ta-N layers are particularly susceptible to the formation of the hex-Ta_2N phase.

3.5. Structure and Bond properties

The RAMAN spectra of the monolithic coatings and the superlattices with $\Lambda_{nom} = 10$ nm are given in Fig. 5. Stoichiometric rock-salt structured high-symmetry materials with all lattice sites occupied generally do not feature first-order vibrational modes. Due to defects such as non-metal vacancies, the order and complete inversion symmetry are disrupted, rendering the material RAMAN-active. For TiC, TiN, and the TiC/TaC SL, two doublets, one in the region between 190 and 370 cm^{-1} (transverse and longitudinal acoustic modes TA and LA) and one between 410 and 660 cm^{-1} (transverse and longitudinal optical modes TO and LO) are present, being consistent with previous studies of TiC and TiN [43,44]. TaC and Ta_2N exhibit a doublet between 80 and 220 cm^{-1} and an optical mode between 560 and 660 cm^{-1}, representing metal-nonmetal interactions; the precise values are listed in Table 2. TiC and the TiC/TaC SL give C–C modes at 1352 and 1575 cm^{-1}, which likely stems from the fact that TiC is over-stoichiometric in carbon, and C–C bonds are inherently RAMAN-active. This suggests that these coatings would also have amorphous-like C-rich grain boundary phases, as no other crystalline phases than those for TiC or TaC could be identified by XRD or SAED during TEM investigations. For TaC and the SLs TiN/TaC and TiC/TaN, the presence of such a C-rich grain-boundary phase can

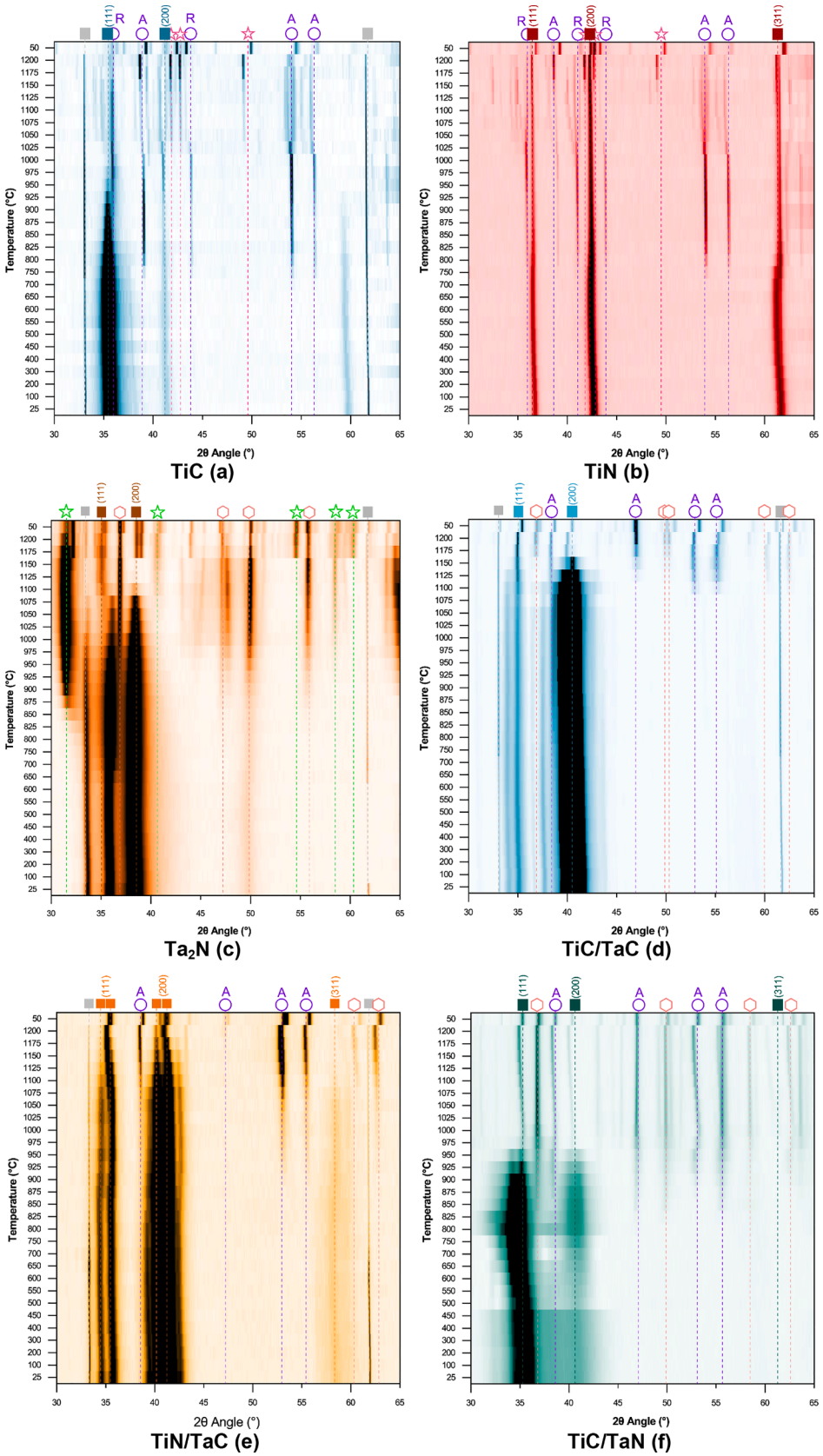

Fig. 4. In-situ XRD investigations under vacuum conditions between 25 °C and 1200 °C for monolithic TiC (a), TiN (b), and Ta_2N (c), and the superlattices TiC/TaC (d), TiN/TaC (e) and TiC/TaN (f). Silicon reflexes are marked in grey, reflexes of the coating itself in a filled square marked with the corresponding miller indices. Oxidation products, and silicides in shapes with white filling ($TiSi_2$: fuchsia star, $TaSi_2$: green star, TiO_2: purple circles marked with A or R for anatase or rutile, Ta_2O_5: orange hexagon). (For interpretation of the references to colour in this figure legend, the reader is referred to the web version of this article.)

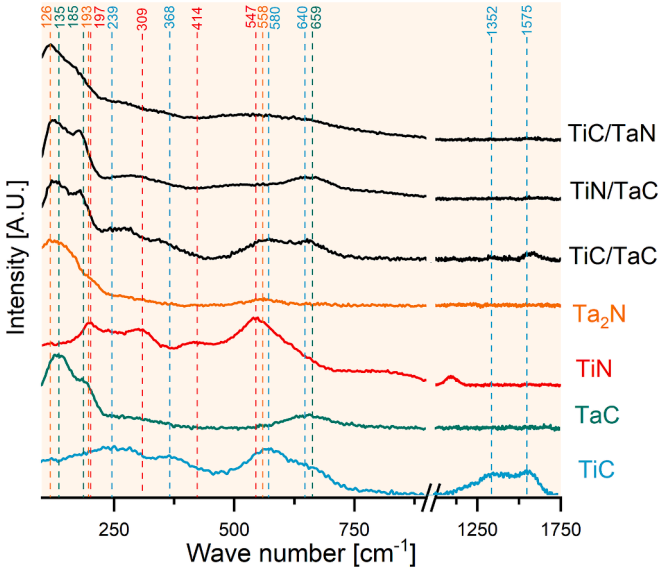

Fig. 5. Raman spectra of the TiC/TaC (a), the TiN/TaC (b), and the TiC/TaN (c) system. The SLs have $\Lambda_{nom} = 10$ nm.

Table 2
Wave numbers and corresponding mode description for transversal (T) and longitudinal (L) acoustic (A) and optical (O) modes.

Mode	TA	LA	TO	LO
TiC	239	368	580	640
TaC	135	185	659	
TiN	197	309	414	547
TaN	126	193	558	

therefore be ruled out, as no such C–C modes are present in their RAMAN spectra, Fig. 5.

3.6. Mechanical properties

3.6.1. Hardness and elastic modulus

TiC/TaC SLs (Fig. 6a) exceed the hardness of their monolithic constituent coatings, TiC and TaC, except for the case of $\Lambda_{nom} = 14$ nm. No clear bilayer dependency is present. The highest hardness ($H = 44.1 \pm 3.4$ GPa) and the lowest hardness ($H = 29.9 \pm 0.9$ GPa) are measured at $\Lambda_{nom} = 2$ nm and $\Lambda_{nom} = 14$ nm, respectively. The TiN/TaC SLs (Fig. 6b) feature higher hardness than their respective monolithic constituents, TiN and TaC, and nearly equate to the hardness of TaC at $\Lambda_{nom} = 2$ and 6 nm. Although H seems to increase with Λ_{nom}, there is no clear trend. The indentation moduli E of TiN/TaC SLs reside in the realm of the monolithic coatings or are even lower (similar for TiC/TaC as well as TiC/TaN).

TiC/TaN SLs (Fig. 6c) exhibit the lowest H and E values out of the here-investigated SL systems. Interestingly, all TiC/TaN SLs are softer than the corresponding monolithic constituents, TiC and Ta_2N. This may be because the monolithic Ta_2N coating is single-phase hexagonal, while the Ta-N layers within the TiC/TaN SL preferably crystallize in the fcc structure. Only for the SLs with $\Lambda_{nom} \geq 28$ nm, also hexagonal Ta_2N phases noticeably contribute to the XRD patterns. The values of the E moduli are generally between those of TiC and Ta_2N, except for the $\Lambda_{nom} = 2$ nm TiC/TaN SL, which exhibits the highest E modulus (also highest H among the TiC/TaN SLs), slightly above that of Ta_2N.

3.6.2. Fracture toughness and residual stresses

The fracture toughness of materials can be determined using different approaches. Within our study, we utilize cube-corner indentation experiments [24]. This technique is relatively quick compared to the fabrication of cantilevers and performing microcantilever bending tests [4,7]. It is necessary to determine residual stresses in the coatings along with the fracture toughness, as the cube-corner-derived fracture toughness can strongly correlate with the stresses [14].

Fig. 7 exemplifies SEM top-view images of cube-corner indents for the same set of samples as analyzed in the previous section. While the monolithic coatings TiC, TaC, TiN, and Ta_2N, Fig. 7a, b, c, and d, respectively, all exhibit pronounced crack formation, the TiN/TaC and

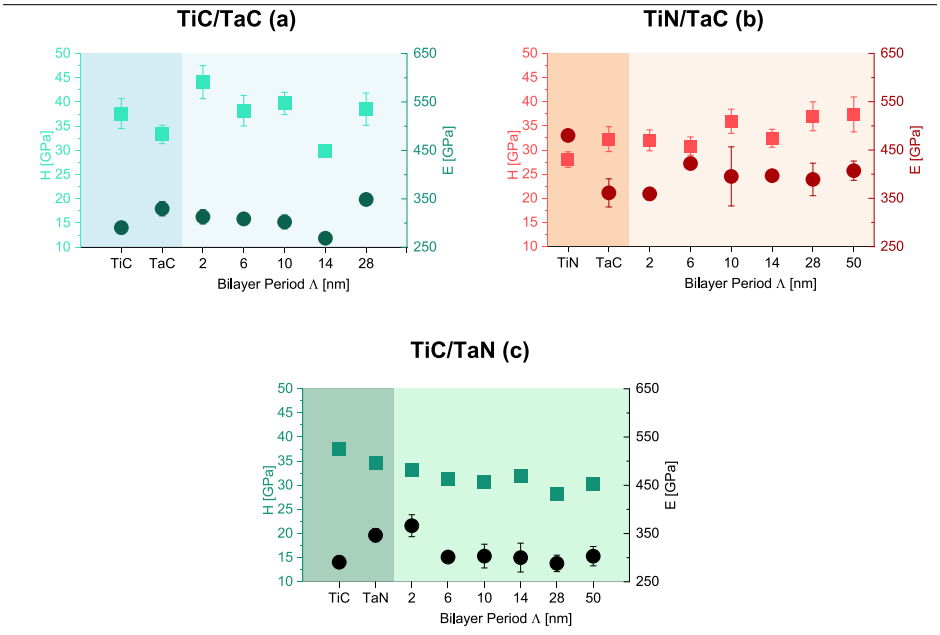

Fig. 6. Hardness (H, light squares) and elastic modulus (E, dark round symbols) for the TiC/TaC (a), TiN/TaC (b), and the TiC/TaN (c) system.

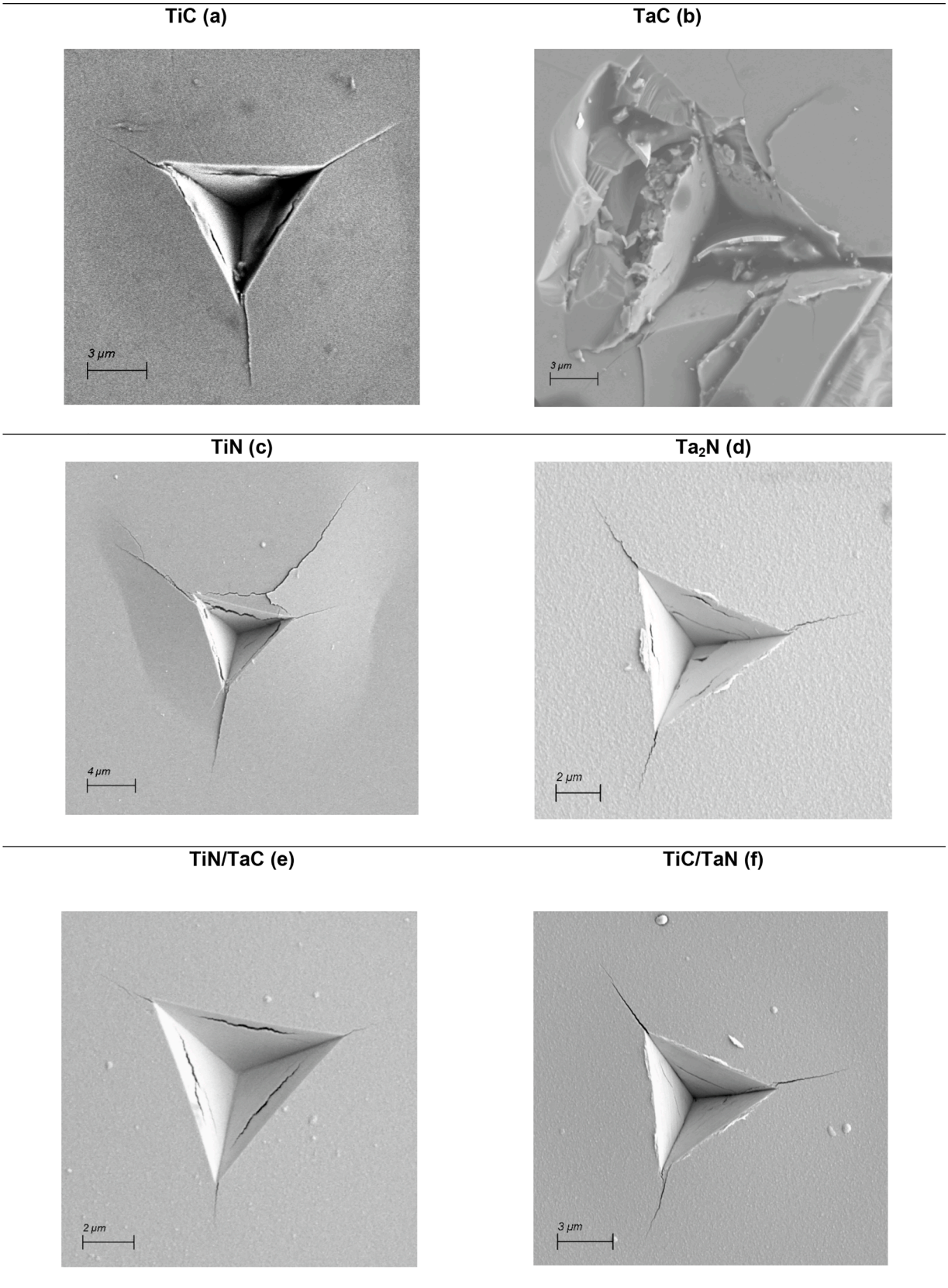

Fig. 7. Cube corner indents on TiC (a), TaC (b), TiN (c), Ta_2N (d) the TiN/TaC $\Lambda_{nom} = 10$ nm superlattice (e) and TiC/TaN $\Lambda_{\mathrm{nom}} = 10$ nm superlattice (f) prepared via cube-corner indentation experiments at a peak force of 450 mN.

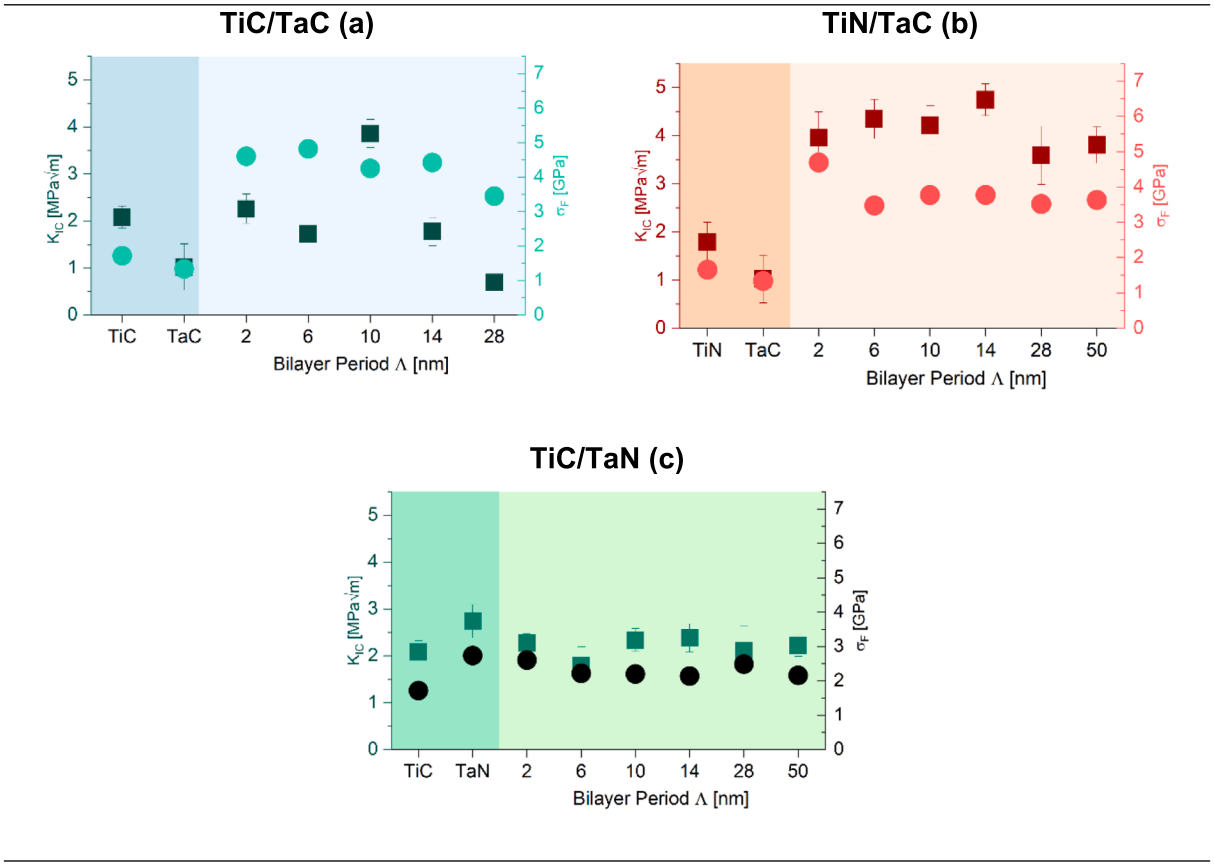

Fig. 8. Fracture toughness and in-plane compressive stresses of both monolithic and superlattice thin films of the TiC/TaC (a), TiN/TaC (b), and TiC/TaN (c) system.

TiC/TaN SLs (Fig. 7e and f) provide a better fracture resistance.

The K_{IC} values of the individual coatings, obtained using Eq. (3) and the crack lengths measured by SEM investigations, are presented in Fig. 8 (and listed in Table 3), together with their biaxial residual stresses. TiN/TaC coatings outperform their constituents with K_{IC} values as high as 4.75 MPa$\sqrt{\text{m}}$ for $\Lambda_{nom} = 14$ and provide an improvement compared to the TiC/TaC SLs (Fig. 8a). Although their residual compressive stresses are even slightly smaller, compare Fig. 8a and b. On the contrary, the TiC/TaN coatings provide lower K_{IC} values (Fig. 8c), although TiC and especially Ta_2N [4] also exhibit a rather good fracture toughness. Table 3 lists the K_{IC} values (fracture toughness) and biaxial residual stresses σ_F, along with the indentation hardness (H), elastic modulus (E), and the H/E ratio—which represents the energy dissipation ability of ceramics.

The monolithic coatings—TiC, TaC, TiN, and Ta_2N—exhibit K_{IC} values between 1.02 ± 0.49 and 2.74 ± 0.36 MPa$\sqrt{\text{m}}$ and biaxial compressive stresses between −1.33 and −2.74 GPa. The ones with higher compressive stress states also have higher K_{IC} values. However, for the SLs, the general picture is not that clear. The TiC/TaC SLs have σ_F values between −4.25 and −4.82 GPa for 2 nm ≤ Λ_{nom} ≤ 14 nm, but their K_{IC} values vary between 1.72 ± 0.16 and 3.85 ± 0.30 MPa$\sqrt{\text{m}}$. There, the maximum K_{IC} is obtained for the 10 nm SL, which exhibits the lowest σ_F among these, Fig. 8 a. Similarly, for the TiN/TaC SLs σ_F only mildly varies between −3.63 and −3.77 GPa, for 6 nm ≤ Λ_{nom} ≤ 50 nm, but K_{IC} varies between 1.72 ± 0.16 and 3.85 ± 0.30 MPa$\sqrt{\text{m}}$. The TiN/TaC SL with Λ_{nom} = 14 nm exhibits the highest K_{IC} value among all coatings studied here, Fig. 8b. For TiC/TaN SLs, the K_{IC} values are essentially between those of the monolithic constituent coatings TiC and Ta_2N. There, the biaxial residual compressive stresses only mildly vary between −2.14 and −2.61 GPa, see Fig. 8c. The comparison of the individual carbide/carbide and nitride/carbide SLs, as well as their monolithic constituents (TiC, TaC, TiN, and Ta_2N), clearly underpins exceptional mechanical properties of TiN/TaC SLs. In particular, their K_{IC} values are three times the rule-of-mixture values of the constituents TiN and TaC, and their H values are beyond the rule-of-mixture.

Table 4 presents the mechanical properties of our superlattices in the context of well-established nitride SLS (including TiN and TaN). The comparison of DFT-derived lattice mismatch and shear modulus mismatch, Δa and ΔG (taken from Ref. [35]) of different TiN- and TaN-containing SL systems, allows correlating their effect on the measured hardness and fracture toughness enhancement (calculated with respect to the harder or more fracture-resistant monolithic material). Recall that Δa and ΔG have been widely seen as the key parameters influencing coherency stresses and varying strain fields at superlattice interfaces, thus hindering the dislocation motion and providing obstacles for crack propagation [47], detailed in the Introduction section.

4. Discussion

Unlike transition metal nitride SLs—being researched already from the 80s (TiN/VN by [8]), with many different systems synthesized and characterized up until today (TiN/WN [5], MoN/TaN [4], TiN/MoN [7], TiN/CrN [46], TiN/TaN [11])—transition metal carbide and carbide/nitride SLs are an almost untouched topic. This might stem from the relatively more challenging synthesis of those ceramic materials. Our results suggest that the combination of hard but relatively brittle carbides with comparably less brittle nitrides may be beneficial for achieving desirable responses to mechanical loads and thermal stability if we can avoid the formation of secondary (unwanted) phases.

For TiC/TaC SLs, a hardness peak was measured at $\Lambda_{nom} = 2$ nm. The obtained $H = 44.1 \pm 3.4$ GPa is significantly above H of the monolithic layer components as well as all other SLs studied here. The TiC/TaC system does not necessarily feature a correlation between the bilayer period and hardness. The lower hardness of the Λ_{nom} = 14 nm coating

Table 3
Hardness (H), E modulus (E), and the H/E values of all monolithic constituents and superlattice structures. Further, experimental apparent fracture toughness (K_{IC}) and experimental in-plane compressive stresses (σ_F) are given.

Material system	Λ_{nom} [nm]	H [GPa]	E [GPa]	H/E [ ]	$K_{IC\ exp}$ [MPa]	σ_F [GPa]
TiC	–	37.6 ± 3.1	290.6 ± 12.6	0.13 ± 0.01	2.08 ± 0.24	1.72
TaC	–	33.3 ± 1.9	329.6 ± 14.9	0.10 ± 0.01	1.02 ± 0.49	1.33
TiN	–	28.0 ± 1.6	480.2 ± 9.0	0.06 ± 0.01	1.79 ± 0.41	1.66
Ta_2N	–	34.6 ± 2.9	346.5 ± 13.7	0.10 ± 0.01	2.74 ± 0.36	2.74
TiC/TaC	2	44.1 ± 3.4	312.9 ± 14.8	0.14 ± 0.01	2.26 ± 0.31	4.60
	6	38.2 ± 3.2	308.7 ± 12.6	0.12 ± 0.01	1.72 ± 0.16	4.82
	10	39.7 ± 2.3	302.3 ± 14.4	0.13 ± 0.01	3.85 ± 0.30	4.25
	14	29.9 ± 0.9	268.7 ± 7.7	0.11 ± 0.01	1.77 ± 0.30	4.42
	28	38.5 ± 3.3	348.7 ± 12.0	0.11 ± 0.01	0.69 ± 0.12	3.45
TiN/TaC	2	32.0 ± 2.2	359.2 ± 12.9	0.09 ± 0.01	3.96 ± 0.53	4.69
	6	30.8 ± 1.9	422.2 ± 12.6	0.07 ± 0.01	4.34 ± 0.41	3.48
	10	36.0 ± 2.5	395.4 ± 30.5	0.09 ± 0.01	4.21 ± 0.41	3.77
	14	32.4 ± 1.9	396.9 ± 10.8	0.08 ± 0.01	4.75 ± 0.33	3.77
	28	37.0 ± 3.0	389.1 ± 33.7	0.10 ± 0.01	3.59 ± 0.61	3.52
	50	37.4 ± 3.6	407.2 ± 20.0	0.09 ± 0.01	3.80 ± 0.38	3.63
TiC/TaN	2	33.1 ± 2.1	366.3 ± 22.8	0.09 ± 0.01	2.27 ± 0.20	2.61
	6	31.3 ± 1.6	301.2 ± 8.1	0.10 ± 0.01	1.80 ± 0.39	2.22
	10	30.6 ± 3.1	303.3 ± 24.6	0.10 ± 0.01	2.33 ± 0.24	2.20
	14	32.0 ± 2.8	300.1 ± 29.9	0.11 ± 0.01	2.38 ± 0.30	2.14
	28	28.3 ± 2.3	288.1 ± 17.0	0.10 ± 0.01	2.11 ± 0.53	2.49
	50	30.2 ± 1.4	303.1 ± 20.0	0.10 ± 0.01	2.22 ± 0.23	2.16

Table 4
Lattice, shear modulus mismatch (Δa and ΔG), together with the hardness- and fracture toughness enhancement (ΔH and ΔK_{IC}) for our superlattice and other nitride systems. Fracture toughness values marked with a * are derived from cantilever bending tests. Therefore, the direct comparison might be challenging; values marked with ** are taken directly from the related publication and might be calculated differently.

Superlattice system	Δa_{DFT} [%] [35]	ΔG_{DFT} [GPa] [35]	ΔH [%] at Λ [nm]		ΔK_{IC} [%] at Λ[nm]	
TiC/TaC	3.2	19	17	2	85	10
TiN/TaC	4.9	25	12	50	141	14
TiC/TaN	1.9	48	–	–	–	–
$TiN/WN_{0.5}$ [5]	1.8	58	15	8.1	53*	10.2
$TiN/MoN_{0.5}$ [7]	0.8	20	4	9.9	46*	9.9
$MoN_{0.5}$/TaN [4]	4.8	35	9**	3	23*,**	5.2

could stem from the slightly higher carbon content compared to other bilayer periods. For TiN/TaC SL, we observed a strong H-dependence on the bilayer period, similar to previously studied VC/ZrC and VC/HfC SLs [14]. However, the TiC/TaN SL coatings also exhibited a bilayer-period-induced change in their phase structure. Specifically, the metastable (high-temperature) cubic phase of TaN [48–50] was stabilized via the template effect at low bilayer periods (note that the bottom layer of TiC/TaN coatings is always 5+ nm thick TiC). The hexagonal Ta_2N phase [52] was especially present within the thicker Ta-N layers, at higher bilayer periods, and/or further away from the substrate interface. The thicker (and/or further away from the substrate interface) the individual Ta-N layers, the higher the fraction of the hexagonal Ta_2N [51,52] phase, and the lower the nitrogen content. Consequently, from $\Lambda_{nom} =$ 10 nm onwards, we observe the formation of a second phase, Ta_2N [51,52]. This second phase seems to destabilize the coating as both hardness and fracture toughness decrease with increasing bilayer periods.

The fracture toughness of TiN/TaC SL shows a maximum of 4.75 ± 0.3 MPa$\sqrt{m}$ at $\Lambda_{nom} = 14$ nm. Consistent with previous studies [14], we observe a linear relationship between the SL bilayer period, their residual stresses, and fracture toughness. The TiC/TaN system does not show a SL-induced enhancement of mechanical properties, but follows a rule-of-mixing type behavior. The presence of two different crystal structures (cubic and hexagonal) in these SLs likely increases the number of grain and phase boundaries and other defects in general. While those could lead to enhanced mechanical properties from hindered gliding of dislocations and their pile-ups, these also interfere with the superlattice effect.

Looking for patterns in hardness and fracture toughness enhancement, we compared our coatings' lattice and shear modulus mismatch with the parameters of established nitride superlattices. While there seems to be no clear trend, SLs with higher shear modulus mismatches tend to exhibit higher hardness and fracture toughness. By comparing our SLs with other systems, we conclude that TiC/TaC and TiN/TaC SLs exhibit excellent enhancement of mechanical properties. It is important to mention that cube-corner-derived fracture toughness and K_{IC} obtained from microcantilever bending tests are not necessarily comparable [11]. In the case of cube corner indentation, the stresses within the coatings can influence the outcome tremendously. At the same time, for cantilever bending tests, the macro stresses are relieved due to the FIB preparation of a free-standing cantilever (where the supporting substrate is removed).

In terms of thermal stability, in-situ XRD investigations revealed a significant increase for both the TiC/TaC and TiN/TaC systems, with the onset of oxidation being 1100 °C. Due to insufficient vacuum conditions, TiO_2 and Ta_2O_5 were able to form. Furthermore, because of the high oxygen affinity of Ti, TiO_2 starts to form earlier than Ta_2O_5 for the TiN/TaC and the TiC/TaC systems. Only the metastable anatase was formed for all SL systems instead of a mixture of anatase and rutile, like for the monolithic TiC and TiN coatings. The similarity of lattice parameters cannot explain this fact, as rutile would be closer to TaC or TaN. Further, no silicides formed in any of the TiC/TaC, TiC/TaN, or TiN/TaC SL coatings, while this is observed for the monolithic TiC, TiN, and Ta_2N coatings, suggesting that the SLs also provide a reduced diffusion and intermixing tendency with the Si substrate.

However, the TiC/TaN system does not feature increased thermal stability, with an onset of oxidation at 800 °C, similar to its constituent materials. This may be attributed to the fact that the study was conducted using a SL coating with $\Lambda_{nom} = 10$ nm. There, the formation of Ta_2N phases introduces additional phase boundaries. This occurses-pecially in the outer layers furthest away from the substrate, which are most susceptible to oxidation. These boundaries and the Ta_2N phase disrupt the SL architecture, promoting diffusion and compromizing oxidation resistance. For this bilayer period, the layers closer to the substrate may not contain the disruptive Ta_2N phase, which could explain why the resistance to disilicide formation remains intact. RAMAN investigations showed no C–C bonds within the films except for carbon over-stoichiometric TiC and the TiC/TaC SLs. As no other crystalline phases than TiC and TaC are observed during XRD of these TiC

and TiC/TaC coatings, this suggests for amorphous-like C-rich grain boundary phases. Generally, the SLs exhibit RAMAN modes of both their constituting materials.

5. Conclusions

Inspired by *ab initio* predictions that highlighted the exceptional fracture resistance of TiN/TaC and TiC/TaN superlattices—standing out among group 4–6 transition metal nitrides and carbides—we present a comparative study of three superlattice (SL) systems: TiN/TaC, TiC/TaN, and TiC/TaC. These systems feature nominal bilayer periods (Λ_{nom}) ranging from 2 to 50 nm.

X-ray diffraction (XRD) analysis confirmed the face-centered cubic (fcc) structure for all coatings, except in SLs with Ta-N layers thicker than 14 nm ($\Lambda_{nom} \geq 28$ nm), where hexagonal Ta_2N phases emerged alongside fcc-TaN. Lattice parameters for the monolithic TiC, TaC, TiN, and Ta-N layers closely match established literature values. Chemical analysis using EBS-ToF-ERDA reveal a near 1:1 metal-to-non-metal ratio in most coatings, with exceptions in monolithic TiC (slightly C over-stoichiometric) and Ta-N (67 at.-% Ta and 33 at.-% N, showing only the Ta_2N phase), and TiC/TaN SLs with $\Lambda_{nom} \geq 28$ nm (where Ta-N layers exhibit a mixed TaN and Ta_2N structure). Raman spectroscopy further confirm the binary nature of all SLs, with C–C interactions in TiC and TiC/TaC SLs stemming from amorphous carbon at grain boundaries.

The mechanical properties of the carbide/nitride SLs, TiN/TaC and TiC/TaN, reveal striking differences. TiN/TaC SLs outperform their monolithic components in terms of hardness, fracture toughness, and thermal stability. The maximum hardness of TiN/TaC SLs ($H = 37.4 \pm 3.6$ GPa at $\Lambda_{nom} = 50$ nm) exceeds that of both constituents, TiN (28.0 ± 1.6 GPa) and TaC (33.3 ± 1.9 GPa). Although the hardness of the TiN/TaC SLs is slightly lower than that of TiC/TaC SLs (which reach $H = 44.1 \pm 3.4$ GPa at $\Lambda_{nom} = 2$ nm), they exhibit superior fracture toughness ($K_{IC} = 4.75 \pm 0.33$ MPa$\sqrt{\text{m}}$ at $\Lambda_{\text{nom}} = 14$ nm), far surpassing TiC/TaC SLs ($K_{IC} = 3.85 \pm 0.30$ MPa$\sqrt{\text{m}}$ at $\Lambda_{nom} = 10$ nm). On the other hand, the TiC/TaN system showed lower hardness ($H = 33.1 \pm 2.1$ GPa at $\Lambda_{nom} = 2$ nm) and fracture toughness ($K_{IC} = 2.38 \pm 0.30$ MPa$\sqrt{\text{m}}$ at $\Lambda_{nom} = 14$ nm) compared to both the monolithic constituents and TiC/TaC SLs.

We demonstrate that the fracture toughness and thermal stability of superhard TiC/TaC superlattices (SLs) can be significantly enhanced—beyond the inherent limits of the SL building blocks—by substituting TiC with TiN, resulting in TiN/TaC SLs. The TiC/TaN SL system shows that achieving optimal mechanical performance is closely tied to maintaining a fully fcc structure, free of secondary phases. In comparing our results across similar SL systems, we find that TiC/TaC offers the highest hardness, while TiN/TaC excels in fracture toughness. With its outstanding combination of thermal stability, hardness, and fracture toughness, the TiN/TaC system outperforms both TiC/TaC and TiC/TaN. Future work would benefit from atomistic simulations to develop a deeper understanding of the observed mechanical properties and extend these findings to other carbide/nitride or even carbonitride nanolaminates.

CRediT authorship contribution statement

Barbara Schmid: Writing – original draft, Visualization, Investigation, Data curation, Conceptualization. **Thomas Schöngruber:** Investigation. **Tomasz Wojcik:** Writing – review & editing, Investigation. **Bálint Hajas:** Investigation. **Eleni Ntemou:** Investigation, Data curation. **Daniel Primetzhofer:** Investigation. **Bernhard Fickl:** Investigation. **Sarah Christine Bermanschläger:** Data curation. **Szilard Kolozsvari:** Resources. **Nikola Koutná:** Writing – review & editing, Supervision, Formal analysis. **Paul Heinz Mayrhofer:** Writing – review & editing, Supervision, Resources, Funding acquisition, Conceptualization.

Declaration of competing interest

The authors declare that they have no known competing financial interests or personal relationships that could have appeared to influence the work reported in this paper.

Acknowledgments

We wholeheartedly want to thank the core facilities at TU Wien, including the XRC (X-Ray Center) for providing XRD and XRF devices and beam time and the USTEM (University Service Centre for Transmission Electron Microscopy) at TU Wien for providing TEM facilities. The authors acknowledge TU Wien Bibliothek for financial support through its Open Access Funding Programme. This work was supported by the RADIATE (Research And Development with Ion Beams – Advancing Technology in Europe) project to provide funding for ERDA and EBS investigations. Further, we want to thank the Tandem Laboratory at the University of Uppsala for cooperating with us on EBS-ERDA investigations.

Data availability

Data will be made available on request.

References

[1] M. Van Stappen, L.M. Stals, M. Kerkhofs, C. Quaeyhaegens, State of the art for the industrial use of ceramic PVD coatings, *Surf. Coat. Technol.* 74–75 (1995) 629–633, https://doi.org/10.1016/0257-8972(95)08296-4.
[2] H. Liang, et al., Insights into the bond behavior and mechanical properties of hafnium carbide under high pressure and high temperature, *Inorg. Chem.* 60 (2) (2021) 515–524, https://doi.org/10.1021/acs.inorgchem.0c02800.
[3] W.G. Fahrenholtz, G.E. Hilmas, Ultra-high temperature ceramics: materials for extreme environments, *Scr. Mater.* 129 (2017) 94–99, https://doi.org/10.1016/j.scriptamat.2016.10.018.
[4] R. Hahn, et al., Mechanistic study of superlattice-enabled high toughness and hardness in MoN/TaN coatings, Commun. Mater. 1 (1) (2020), https://doi.org/10.1038/s43246-020-00064-4.
[5] J. Buchinger, et al., Toughness enhancement in TiN/WN superlattice thin films, *Acta Mater.* 172 (2019) 18–29, https://doi.org/10.1016/j.actamat.2019.04.028.
[6] P.B. Mirkarimi, L. Hultman, S.A. Barnett, Enhanced hardness in lattice-matched single-crystal TiN/$V_{0.6}Nb_{0.4}$N superlattices, Appl. Phys. Lett. 2654 (June) (1998) 1–4.
[7] Z. Gao, J. Buchinger, N. Koutná, T. Wojcik, R. Hahn, P.H. Mayrhofer, Ab initio supported development of TiN/MoN superlattice thin films with improved hardness and toughness, *Acta Mater.* 231 (2022) 117871, https://doi.org/10.1016/j.actamat.2022.117871.
[8] X. Chu, S.A. Barnett, Model of superlattice yield stress and hardness enhancements, *J. Appl. Phys.* 77 (9) (1995) 4403–4411, https://doi.org/10.1063/1.359467.
[9] U. Helmersson, S. Todorova, S.A. Barnett, J. Sundgren, Growth of single-crystal TiN/VN slrained-layer superlattices with extremely high mechanical hardness, J. Appl. Phys. 481 (1987) (2003) 1–5.
[10] X.C. Dong, J.L. Yue, E.Q. Wang, M.L. Li, G.Y. Li, Microstructure and superhardness effect of VC/TiC superlattice films, *Trans. Nonferrous Met. Soc. China (English Ed.)* 25 (8) (2015) 2581–2586, https://doi.org/10.1016/S1003-6326(15)63878-X.
[11] P.H. Mayrhofer, H. Clemens, F.D. Fischer, Materials science-based guidelines to devel-op robust hard thin film materials, *Prog. Mater. Sci.* 146 (2024) 101323, 1–57. https://doi.org/10.1016/j.pmatsci.2024.101323.
[13] B. Schmid, N. Koutná, R. Hahn, T. Wojcik, P. Polcik, P.H. Mayrhofer, Development of TaC-based transition metal carbide superlattices via compound target magnetron sputtering, Int. J. Refract. Metals Hard Mater 113 (March) (2023), https://doi.org/10.1016/j.ijrmhm.2023.106165.
[14] B. Schmid, et al., Mechanical properties of VC/ZrC and VC/HfC superlattices, *Acta Mater.* 270 (2024), https://doi.org/10.1016/j.actamat.2024.119852.
[15] M. Deutsch, et al., X-ray spectrometry of copper: new results on an old subject, *J. Res. Nat. Inst. Stand. Technol.* 109 (1) (2004) 75, https://doi.org/10.6028/jres.109.006.
[16] P.J. Withers, M. Preuss, A. Steuwer, J.W.L. Pang, Methods for obtaining the strain-free lattice parameter when using diffraction to determine residual stress, *J. Appl. Cryst.* 40 (5) (2007) 891–904, https://doi.org/10.1107/S0021889807030269.
[17] P. Ström, D. Primetzhofer, Ion beam tools for nondestructive in-situ and in-operando composition analysis and modification of materials at the Tandem Laboratory in Uppsala, *J. Instrument.* 17 (4) (2022), https://doi.org/10.1088/1748-0221/17/04/P04011.
[18] M.S. Janson. "CONTES Conversion of Time-Energy- Spectra-A Program for ERDA Data Analysis Users Manua," Uppsala, 2004.
[19] M. to Baben, M. Hans, D. Primetzhofer, S. Evertz, H. Ruess, J.M. Schneider, Unprecedented thermal stability of inherently metastable titanium aluminum

nitride by point defect engineering, *Mater. Res. Lett.* 5 (3) (2017) 158–169, https://doi.org/10.1080/21663831.2016.1233914.
[20] A.F. Gurbich, SigmaCalc recent development and present status of the evaluated cross-sections for IBA, *Nucl. Instrum. Methods Phys. Res. B* 371 (2016) 27–32, https://doi.org/10.1016/j.nimb.2015.09.035.
[21] M. Mayer, Improved physics in SIMNRA 7, *Nucl. Instrum. Methods Phys. Res. B* 332 (2014) 176–180, https://doi.org/10.1016/j.nimb.2014.02.056.
[22] A.C. Fischer-Cripps, Critical review of analysis and interpretation of nanoindentation test data, *Surf. Coat. Technol.* 200 (14–15) (2006) 4153–4165, https://doi.org/10.1016/j.surfcoat.2005.03.018.
[23] E. Tarrés, G. Ramírez, Y. Gaillard, E. Jiménez-Piqué, L. Llanes, Contact fatigue behavior of PVD-coated hardmetals, *Int. J. Refract. Metals Hard Mater.* 27 (2) (2009) 323–331, https://doi.org/10.1016/j.ijrmhm.2008.05.003.
[24] T. Zhang, Y. Feng, R. Yang, P. Jiang, A method to determine fracture toughness using cube-corner indentation, *Scr. Mater.* 62 (4) (2010) 199–201, https://doi.org/10.1016/j.scriptamat.2009.10.025.
[25] A. Kirnbauer, et al., Mechanical properties and thermal stability of reactively sputtered multi-principal-metal Hf-Ta-Ti-V-Zr nitrides, *Surf. Coat. Technol.* 389 (February) (2020) 125674, https://doi.org/10.1016/j.surfcoat.2020.125674.
[26] E. Chason, "Resolution and sensitivity of stress measurements with the k-Space Multi-beam Optical Sensor (MOS) System," pp. 1–11, 2004, [Online]. Available: http://www.k-space.com/pdfs/kSA_MOS_Resolution.pdf.
[27] K. Frisk, Analysis of the phase diagram and thermochemistry in the Ta–N and the Ta–C–N systems, *J. Alloy. Compd.* 278 (1–2) (1998) 216–226, https://doi.org/10.1016/S0925-8388(98)00582-9.
[28] M. Fallmann, Z. Chen, Z.L. Zhang, P.H. Mayrhofer, M. Bartosik, Mechanical properties and epitaxial growth of TiN/AlN superlattices, *Surf. Coat. Technol.* 375 (2019) 1–7, https://doi.org/10.1016/j.surfcoat.2019.07.003.
[29] N. Koutná, et al., Atomistic mechanisms underlying plasticity and crack growth in ceramics : a case study of AlN / TiN superlattices, *Acta Mater.* 229 (2022), https://doi.org/10.1016/j.actamat.2022.117809.
[30] N. Koutná, et al., Point-defect engineering of MoN/TaN superlattice films: a first-principles and experimental study, *Mater. Des.* 186 (2020) 108211, https://doi.org/10.1016/j.matdes.2019.108211.
[33] J.F. Shackelford, Y.-H. Han, S. Kim, S.-H. Kwon, *Crc Materials Science and Engineering Handbook; Fourth Edition*, Fourth Edition. doi: 10.4324/9780429130687.
[34] K. Aigner, W. Lengauer, D. Rafaja, P. Ettmayer, Lattice parameters and thermal expansion of Ti(CxN1-x), Zr(CxN1-x), Hf(CxN1-x) and TiN1-x from 298 to 1473 K as investigated by high-temperature X-ray diffraction, *J. Alloy. Compd.* 215 (1–2) (1994) 121–126, https://doi.org/10.1016/0925-8388(94)90828-1.
[35] N. Koutná, A. Brenner, D. Holec, P.H. Mayrhofer, High-throughput first-principles search for ceramic superlattices with improved ductility and fracture resistance, *Acta Mater.* 206 (March 2021) (2021) 1–17, https://doi.org/10.1016/j.actamat.2020.116615.
[36] R.W.G. Wyckoff, *Crystal Structures: 1*, secondnd ed., Interscience Publishers, New York, 1963.
[37] N. Terao, Structure of tantalum nitrides, *Jpn. J. Appl. Phys.* 10 (2) (1971) 248–259, https://doi.org/10.1143/JJAP.10.248.
[38] D.A.H. Hanaor, C.C. Sorrell. "Review of the anatase to rutile phase transformation," Feb. 2011. doi: 10.1007/s10853-010-5113-0.
[39] V. Vijay, S. Bhuvaneswari, V.M. Biju, R. Devasia, Influence of titanium silicide active filler on the microstructure evolution of borosiloxane-derived Si-B-O-C ceramics, *J. Ceram. Sci. Technol.* 7 (1) (2016) 97–106, https://doi.org/10.4416/JCST2015-00040.
[40] S. Lei, et al., Diffusion barrier effect of Ta or TaSi2 layer at the MoSi2/Nb-based alloy interface, *Corros. Sci.* 216 (2023), https://doi.org/10.1016/j.corsci.2023.111090.
[41] A.V. Nomoev, S.P. Bardakhanov, M. Schreiber, D.Z. Bazarova, B.B. Baldanov, N. A. Romanov, Synthesis, characterization, and mechanism of formation of janus-like nanoparticles of tantalum silicide-silicon (TaSi2/Si), *Nanomaterials* 5 (1) (2014) 26–35, https://doi.org/10.3390/nano5010026.
[42] W.S. Chen, H.J. Ho, K.Y. Lin, Hydrometallurgical process for tantalum recovery from epoxy-coated solid electrolyte tantalum capacitors, Materials 12 (8) (2019), https://doi.org/10.3390/ma12081220.
[43] N. Saoula, et al., Study of the deposition of Ti/TiN multilayers by magnetron sputtering, *Surf. Interface Anal.* 42 (6–7) (2010) 1176–1179, https://doi.org/10.1002/sia.3299.
[44] C. Poltorak, M. Stüber, H. Leiste, A. Bergmaier, S. Ulrich, Study of (Ti,Zr)C:H/a-C:H nanocomposite thin film formation by low temperature reactive high power impulse magnetron sputtering, *Surf. Coat. Technol.* 398 (February) (2020) 125958, https://doi.org/10.1016/j.surfcoat.2020.125958.
[46] R. Hahn, M. Bartosik, R. Soler, C. Kirchlechner, G. Dehm, P.H. Mayrhofer, Superlattice effect for enhanced fracture toughness of hard coatings, *Scr. Mater.* 124 (2016) 67–70, https://doi.org/10.1016/j.scriptamat.2016.06.030.
[47] J. Buchinger, et al., Fracture toughness trends of modulus-matched TiN/(Cr,Al)N thin film superlattices, *Acta Mater.* 202 (January) (2021) 376–386, https://doi.org/10.1016/j.actamat.2020.10.068.
[48] C. Stampfl, A.J. Freeman, Metallic to insulating nature of (formula presented) Role of Ta and N vacancies, *Phys. Rev. B Condens. Matter Mater. Phys.* 67 (6) (2003), https://doi.org/10.1103/PhysRevB.67.064108.
[49] N. Koutná, D. Holec, O. Svoboda, F.F. Klimashin, P.H. Mayrhofer, Point defects stabilise cubic Mo-N and Ta-N, *J. Phys. D Appl. Phys.* 49 (37) (2016), https://doi.org/10.1088/0022-3727/49/37/375303.
[50] C.S. Shin, et al., Growth and physical properties of epitaxial metastable cubic TaN (001), *Appl. Phys. Lett.* 75 (24) (1999) 3808–3810, https://doi.org/10.1063/1.125463.
[51] L. Rivaud, S.A. Barnett, J.E. Greene, E.T. Marciniec, Structure and physical properties of polycrystalline hexagonal Ta2N films deposited by reactive sputtering, *J. Vac. Sci. Technol. A* 9 (4) (1991) 2180–2182, https://doi.org/10.1116/1.577247.
[52] T. Chihi, J.C. Parlebas, M. Guemmaz, First principles study of structural, elastic, electronic and optical properties of Nb2N and Ta2N compounds, *Phys. Status Solidi B Basic Res.* 248 (12) (2011) 2787–2792, https://doi.org/10.1002/pssb.201147033.

Further reading

[12] Q.Q. Bai, Y. Bai. "12 Fatigue and Fracture," in *Subsea Pipeline Design, Analysis, and Installation*, 2014, ch. 12, pp. 283–318. doi: 10.1016/B978-0-12-386888-6.00012-2.
[31] H. Riedl, et al., Influence of carbon deficiency on phase formation and thermal stability of super-hard TaCy thin films, *Scr. Mater.* 149 (2018) 150–154, https://doi.org/10.1016/j.scriptamat.2018.02.030.
[32] R.O.E. Vijgen, J.H. Dautzenberg. "Mechanical measurement of the residual stress in thin PVD films," 1995.
[45] S. Pellegrino, L. Thomé, A. Debelle, S. Miro, P. Trocellier, Radiation effects in carbides: TiC and ZrC versus SiC, *Nucl. Instrum. Methods Phys. Res. B* 327 (1) (2014) 103–107, https://doi.org/10.1016/j.nimb.2013.11.046.